RESEARCH ARTICLE

Computational Design and Thermal Properties of Reverse Hybrid Core–Shell Nanoparticles for Photothermal Therapy Applications

Fereshteh Shafiepour [1], Somayeh Salmani Shik [1,2,*], Armin Aminimajd [3], Mohammad H. Majles Ara [1,2]

ABSTRACT: The efficacy of Hyperthermia treatment hinges on the strategic selection of the heating agents. Marking a pioneering advancement in this field, we introduce the simulation of Reverse Hybrid Core-Shell Nanoparticles (NPs) based on Gold Nanorods (AuNRs) as core and $SiO_2@Fe_3O_4$ as shell due to their superior optical, thermal, and magnetic properties for enhanced hyperthermia applications and NPs targeting. Using COMSOL Multiphysics, employing the RF Module and Heat Transfer in Solid Module, we meticulously calculated the Optical Cross-Sections and Thermal Profiles of various hybrid NP configurations. Our investigation spanned a range of core and shell dimensions, including 50, 60, and 70 nm SiO_2 thicknesses with 10 and 15 nm Fe_3O_4 layers, coupled with two core dimensions of 10 nm × 41 nm and 15 nm × 52.5 nm AuNRs. The results indicate that the λ_{SPR} of different hybrid NPs experiences a redshift by 50-80 nm compared to the λ_{SPR} of single AuNR. Leveraging the Q_{abs} of three distinct hybrid NPs, resulted from RF model, and obtaining the thermal distribution profiles of them, we demonstrate that the addition of optimized shell- 60 nm $SiO_2@10$ nm Fe_3O_4- reduces the temperature of the hybrid NPs with smaller AuNR core and the larger AuNR core from 56.4 ℃ (for the single AuNR) to 41.9 ℃ (AuNR with shell) and from 70.8 ℃ to 47.2 ℃, respectively. As a result, the 15 nm × 52.5 nm AuNR@ 60 nm $SiO_2@$ 10 nm Fe_3O_4 hybrid core-shell NP with λ_{SPR}=840 nm can be a proper candidate for photothermal therapy.

Keywords: Gold Nanorods (AuNRs), Core-Shell Nanoparticles, Hyperthermia, Magnetic NPs, COMSOL Multiphysics

1. INTRODUCTION

In the past few years, innovative methods have emerged as substitutes for treating tumors. Several of these methods are designed to induce hyperthermia, a prosses where tissue is warmed to temperatures ranging from 41 to 47 degrees Celsius and maintained for a duration of 20 to 30 minutes [1-3]. Lately, treatment strategies utilizing the near infrared (NIR) spectrum, like photothermal therapy (PTT), have gained traction owing to their superior ability to penetrate biological tissues. PTT is emerging as a leading-edge option for cancer therapy, utilizing light's energy to target and eliminate cancer cells effectively and non-invasively [4-6]. The distinction between traditional hyperthermia and photothermal therapy lies in the fact that generated photothermal heating is in the vicinity of the agents used in PTT, known as photothermal agents (PTAs). This localized heating can elevate temperatures significantly, reaching levels several tens or even hundreds of degrees higher than the body's normal temperature, and this occurs within extremely brief periods. This shows that photothermal heating has the potential to be more precisely directed at tumor cells instead of normal cells [7]. The principle behind this technique is the phenomenon of surface plasmon resonance (SPR) [8, 9]. SPR phenomenon takes place when electrons on an agent's surface collectively oscillate upon interacting with incoming light. This process results in the

[1] Nanophysics Lab, Faculty of Physics, Kharazmi University, Tehran, Iran.

[2] Applied Sciences Research Center, Kharazmi University, Tehran, Iran.

[3] Macromolecular Science and Engineering Department, Case Western Reserve University, Ohio, USA.

*Author to whom correspondence should be addressed:
salmani@khu.ac.ir (S. Salmani Shik)

agent absorbing the light and transforming it into heat, which is then utilized to increase the temperature of specific tissues [10-12]. PTAs fall into different groups, for instance: Carbon Nanostructures, which encompass materials like graphene and carbon nanotubes, among other carbon derivatives [4,5], Noble Metal Nanostructures, with a particular emphasis on nanoparticles made of gold [13-17] and silver [17-20], transition metal sulfides (such as tungsten disulfide (WS$_2$) [21,22] and molybdenum disulfide (MoS$_2$) [23,24]), organic polymers such as porphyrin [25,26], and other nanostructures such as hybrid core-shell nanoparticles [27].

Metal based compounds, including structures based on gold (Au) and silver (Ag), are widely recognized as the most prominent photothermal agents. Their unique properties, such as low cytotoxicity and excellent biocompatibility, make them stand out. Additionally, they can be readily synthesized and modified for specific uses. In contrast to Ag NPs, Au NPs exhibit greater stability in ambient condition. [13-20] Nanoparticle dimensions, morphology, and concentration significantly impact their interactions within biological systems and therapeutic results. Research indicates that modifying these characteristics can influence the SPR wavelength, the light absorption rate, and thermotherapy temperature of nanoparticles [28, 29]. In this regards, Rituraj Borah et al. studied the optical response of different gold nanoparticles (GNPs) clusters sizes (20 nm and 40 nm). They showed that for clusters of nanoparticles measuring 20 nm with a narrow gap between particles (1 nm), which result in intense near-field interaction, the per particle absorption intensity grows as the cluster size expands [30].

Compared to GNPs, it has been shown that gold nanorods (GNRs) exhibit remarkable suitability for photothermal therapy due to robust SPR effects in the near-infrared spectrum, enabling deeper tissue penetration and efficient heat production. For example, Alrahili et al. studied 4 types of GNMs, 20 nm Au nanoparticles (AuNPs), 80 nm gold nanourchins (GNUs), and two gold nanorods with different aspect ratios (25 nm × 60 nm GNRs and 10 nm × 41 nm GNRs). The results indicated that the SPR wavelength of 10 nm × 41 nm GNR is about 808nm which matches the wavelength of the IR light used for PTT, leading to absorb more lights and rapidly convert it to heat due to the absorption being in sync with the laser's wavelength (λ_{SPR}= 808 nm) [31].

Besides gold NPs, there is a significant use of magnetic iron oxide NPs (IONPs), particularly those derived from Fe$_3$O$_4$ [32], in the application of magnetic hyperthermia. These magnetic NPs (MNPs) have the property of aligning their magnetic moment with an external magnetic field. Such alignment leads to the MNPs being drawn towards the area where the magnetic field gradient is applied. Consequently, integrating both types of NPs- plasmonic NPs for thermal effect and generating heat and MNPs for precise targeting-into a single NP structure is highly appealing for advanced therapeutic applications. [27-33]

While most of the research on hybrid magnetic-plasmonic NPs for biomedical uses typically focuses on IONPs encased in Au shell, our study investigates an alternative NP structure. In our work, Au core is encased by IONPs. Utilizing pre-manufactured gold NPs allows for more precise regulation of the localized surface plasmon resonance, which is crucial for photothermal therapy. In this study, using the COMSOL Multiphysics, we conduct a comprehensive simulation of Hybrid Core-Shell NPs with AuNR core and SiO$_2$@Fe$_3$O$_4$ shell to determine their Absorption Cross-Section (σ_{abs}), Scattering Cross-Section (σ_{sct}), and Extinction Cross-Section (σ_{ext}). Additionally, we extend our investigation to include Thermal Profiles of a single AuNR and a core-shell structure based on the AuNR. The comparative analysis aims to elucidate the impact of different core and shell sizes on the absorption efficiency and resultant temperature distribution, providing insights into the design of the proper hybrid core-shell NPs for targeted applications in photothermal therapy.

2. METHODS

In the current research, we employed hybrid core-shell nanoparticles featuring an Au Nanorod core, with optical constants derived from Johnson and Christy, and a coating of SiO$_2$@Fe$_3$O$_4$ shell of varying thicknesses, utilizing optical constants for Fe$_3$O$_4$ as reported by Querry1985 (Figure 1).

Our core-shell NP configurations maintain a size below 100 nm, as particles within this size range demonstrate superior structural and functional characteristics [33]. Additionally, the study encompassed an analysis of the temperature gradient generated in the aqueous surrounding medium. The computational method's validity is corroborated by established literature [31]. For model validation, the surface plasmon resonance wavelength λ_{SPR} of 10 nm × 41 nm AuNR (λ_{SPR}=808 nm), was found to be in close alignment with the experimental findings reported in literature, as detailed in Section 3.1. Subsequent phases involved determining the λ_{SPR} and temperature variations of the hybrid core-shell nanoparticles across different core and shell dimensions. The methodology comprised a two-step process: initially, the RF Module calculated the energy absorption, followed by the Heat Transfer in Solids module, which solved the heat equation using the absorbed power per unit volume data as the heat source [31]. This approach enabled the precise calculation of temperature fluctuations near each nanoparticle.

2.1. Optical quantities using RF Module

In this investigation, the finite element method (FEM) was utilized through the COMSOL Multiphysics simulation platform, alongside the RF Module operating within the frequency domain, to solve Maxwell's equations. Within this specific module, Maxwell's equations are formulated as a wave equation governing the electric field, as referenced in [28, 31]:

$$(\nabla \times E) - k_0^2 \varepsilon E = 0 \tag{1}$$

Where μ_r denotes the relative permeability of the material in question, E represents the electric field, k_0 is the wave propagation vector, and ε signifies the dielectric permittivity of the material, encompassing both its real and imaginary components. The displacement field model employed herein is predicated upon the refractive index of the material.

Within the COMSOL simulation environment, electromagnetic waves can be resolved through two distinct formulations: the Full Field and the Scattered Field approaches. The Full Field formulation necessitates the specification of an input port, direction, and location for the input field. However, given that our module operates within an infinite domain, the Scattered Field formulation was adopted, wherein the input field is applied across the entire simulation domain. Consequently, a plane wave, polarized along the x-axis and advancing along the z-axis, is established as per reference [31]:

$$E_b = E_0 e^{(-j\frac{2\pi n}{\lambda}z)\hat{\imath}} \tag{2}$$

With E_0 being the amplitude of the wave (1 V/m), n the refractive index of the medium (in case, water, n=1.33), and λ the wavelength (400-1100 nm in our study). Figure 2 shows E_b and the background magnetic field (H_b) in different directions.

To mitigate the boundary reflections within the computational domain, a perfectly matched layer (PML) was constructed encircling the physical domain-comprising both the nanoparticle and its immediate environment-with a thickness of $\lambda_{max}/2$. This layer serves to effectively curtail the computational space while minimizing the introduction of

artifacts into the solution. Additionally, a scattering boundary condition was applied to the domain's periphery, ensuring that waves impinging upon the computational boundary do not reflect into the central domain of interest [34]. Due to using a symmetric geometry, a perfect electric conductor and a perfect magnetic conductor were applied in specific areas. The first mesh applied to the system was physics controlled with an extremely fine size. Applying three other sizes on the nanoparticle domain and boundaries, we improved the accuracy of our mesh. All domains and boundary conditions are depicted Figure 3.

The geometrical parameters that measure the absorption, scattering, and extinction properties of a material are known as the absorption cross-section, scattering cross-section, and extinction cross-section, respectively. These parameters are mathematically defined in references [33,34-36]:

$$\sigma_{abs}[m^2] = 4 \times \frac{W_{abs}[W]}{S_I\left[\frac{W}{m^2}\right]} , \sigma_{sca} = 4 \times \frac{W_{sca}}{S_I},$$

$$\sigma_{ext} = \sigma_{abs} + \sigma_{sca} \tag{3}$$

where W_{abs} and W_{sca} are the energies absorbed and scattered by the nanoparticle, respectively, and S_I is the intensity of input light (power per unit area). The operation was multiple 4 to calculate the result in the whole geometry.

$$S_I = \frac{1}{2}c\varepsilon_0|E_0|^2\hat{k} \tag{4}$$

In the equations presented c represents the speed of light in vacuum and ε_0 stands for the vacuum permittivity, respectively. The symbol k^ indicates the direction of propagation of the incoming light wave.
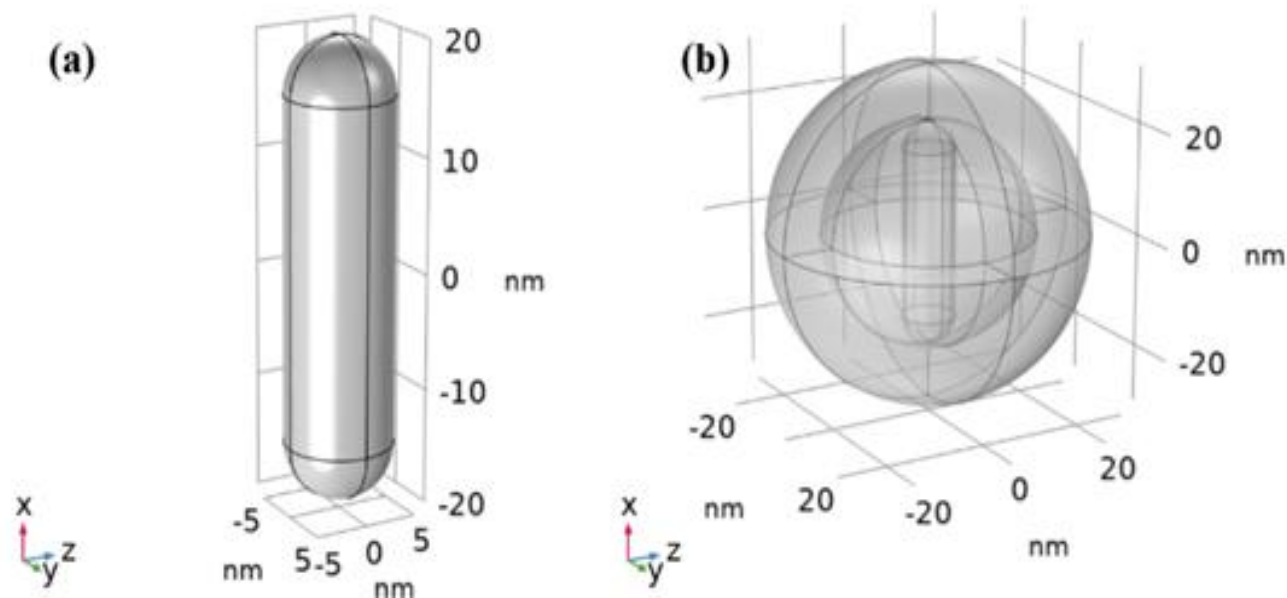
Fig. 1. a) 10nm × 41nm AuNR with major axis (longitudinal) along with X-axis. b) The hybrid core–shell nanoparticle with AuNR core and $SiO_2@Fe_3O_4$ shell.
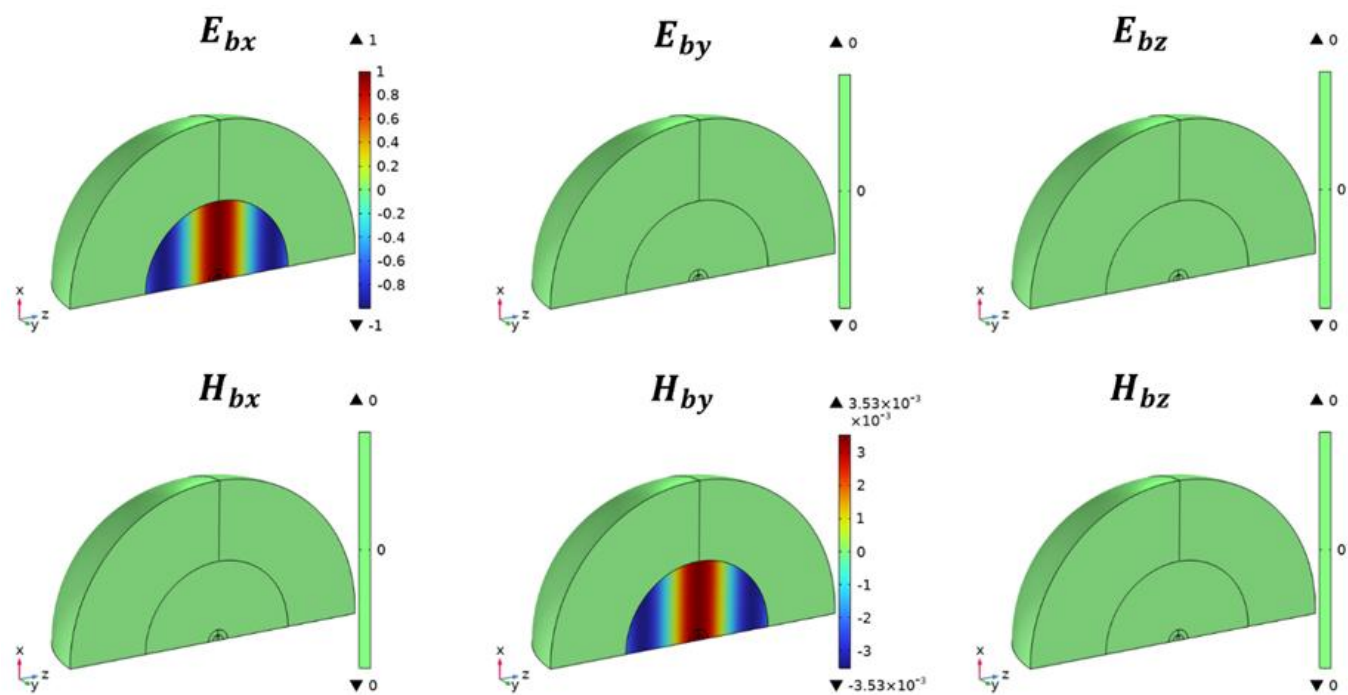
Fig. 2. The background Electric and Magnetic field polarized along x-axis and propagating along the z-axis
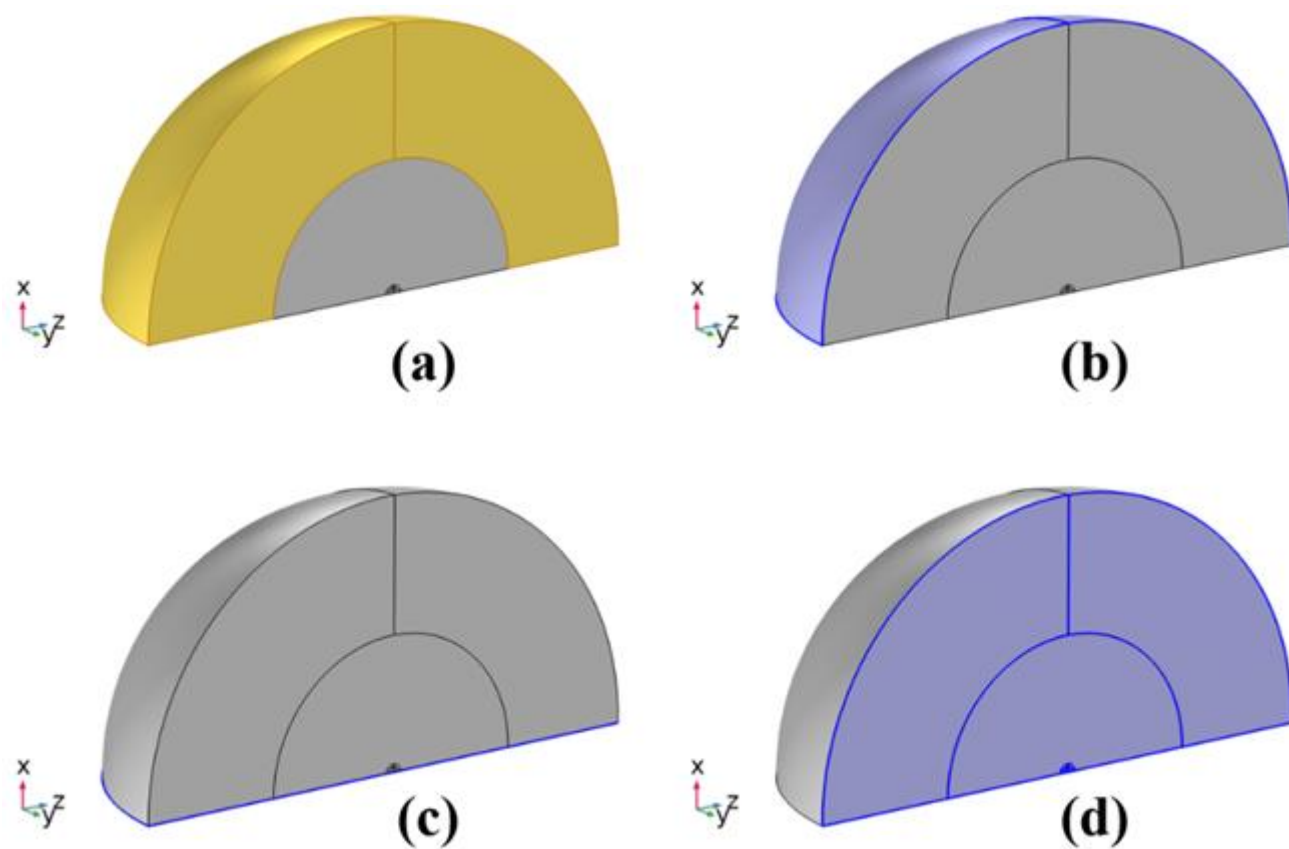
Fig. 3. (a) The PML around the hybrid core-shell nanoparticle for domain truncation in RF module computation, (b) the scattering boundary condition on the outermost surface, (c) the Perfect Electric Conductor, and (d) the Perfect Magnetic Conductor boundary conditions.

The numerical solution provides the values for the power absorbed and scattered as delineated in eq.3 [28]:

$$W_{abs} = \frac{1}{2} \iiint_v \; Re[(\sigma E + j\omega D)E^* + j\omega BH^*]dV \qquad (5)$$

$$W_{sca} = \frac{1}{2} \iiint_s \; Re[E_{sca} \times H_{sca}^*]ndS \qquad (6)$$

In the aforementioned expressions, D signifies the displacement currents signifies the displacement currents * represents the complex conjugate, respectively. In eq.5, the volume integration is throughout the entire nanoparticle, and in eq.6, the surface integral is specifically over the nanoparticle's surface. The energy absorption by the nanoparticles can be efficiently determined within COMSOL by performing an integration of the power dissipation density across the nanoparticle's volume [31]:

$$W_{abs} = \iiint_\Omega \; Q_h d\Omega \qquad (7)$$

In the context of this study, Q_h is designated as the variable within COMSOL that quantifies the power dissipation density. Owing to its wavelength (λ) dependency, a parametric analysis was conducted across a spectrum of λ values to ascertain the optical cross-section spectra. Furthermore, the quantification of the energy dispersed by the nanoparticles is accomplished in COMSOL through the integration of the Poynting vector across the nanoparticle's surface.

2.2 Heat Transfer in Solids module

2.2.1. Calculating the Heat Source Power of a Hybrid Core–Shell Nanoparticle

The nanoparticles absorption characteristics play an important role in the context of photothermal heating. At the λ_{SPR}, the absorption of light is at its peak, which in turn maximizes the photothermal heating produced by NPs. The computation of photothermal heating, especially for nanoparticles with complex geometries, is effectively estimated by an equation based on the W_{abs} and the nanoparticle's volume [34]:

$$Q_{abs} = \frac{W_{abs}}{V} \qquad (8)$$

In this context, Q_{abs} [w/m^3] is defined as the power produced by the nanoparticle per unit of volume.

2.2.2. Heat Transfer Analysis for Hybrid Core-Shell Nanoparticle in a Homogeneous Environment

For the heat transfer analysis, we utilized the Heat Transfer in Solids module of COMSOL, which incorporated a localized heat source Q_{abs} within the hybrid core-shell

nanoparticle. The temperature, denoted as T, was the dependent variable in this model. A stationary study was conducted to determine the maximum temperature increase within the system, and the steady-state heat equation is expressed as follows in references [28,31,33,35]:

$$\rho c_p \, \partial T - k\nabla^2 T = Q_{abs} \qquad (9)$$

Where k [W/(m.K)] denotes the thermal conductivity, ρ represents the density, and c_p is the specific heat capacity at constant pressure for the medium, such as water, which is detailed in Table 1. The initial temperature of the nanoparticle is established at human body temperature, which is 37 °C.

Given that our study does not involve the propagation of waves, the use of a Perfectly Matched Layer (PML) is rendered unnecessary. Instead, a sphere with a diameter of 3µm is positioned around the nanoparticle to simulate the surrounding medium, and a constant temperature boundary condition of 37 °C is applied to the furthest boundaries of the system.

Table 1. The thermal conductivity k, density ρ, and specific heat capacity at constant pressure c_p of materials.

Material	k (W/(m.K))	ρ (kg/m^3)	c_p (J/(kg.K))
Gold [35]	318	19300	129
Water [35]	0.6	1000	4200
SiO$_2$ (polycrystalline) [39]	1.3	COMSOL function	COMSOL function
Fe$_3$O$_4$ [40]	4.9	COMSOL function	COMSOL function

3. RESULTS AND DISCUSSION

3.1. Validation of the computational model

The computational model was validated by the results obtained experimentally from literature for 10 nm × 41 nm AuNR with λ_{SPR}=808 nm [31]. In Figure 4 it can be seen that plasmon resonance wavelengths are similar between the experimental result and the simulated (λ_{SPR}=808 nm). Nonetheless, the variability in experimental samples, which include particles with diverse sizes, shapes, and orientations, in addition to clusters formed during synthesis, results in a difference in the experimental spectra peak (~0.7) compared to what is seen in simulation (~1.8). We also obtained the Field Enhancement [V/m] and the Power Dissipation Density, Q_h [w/m^3], to contrast them with other geometries acquired for subsequent analysis. The results can be seen in Figure 5.
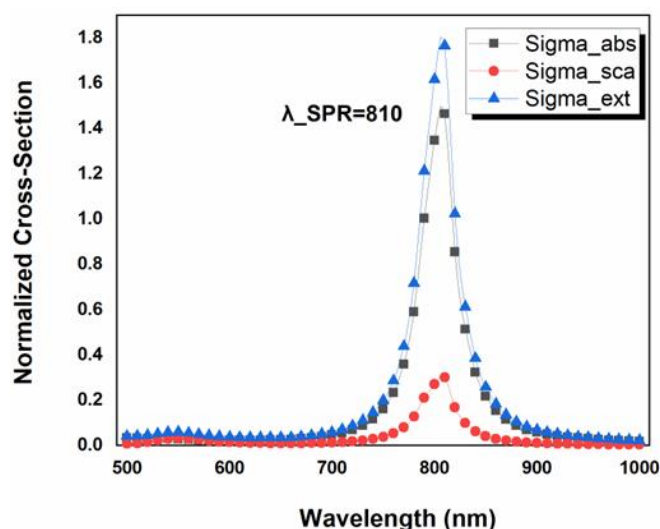
Fig. 4. The normalized absorption, scattering, and the extinction cross-section for 10nm × 41nm AuNR with λ_{SPR}= 810 nm simulated.

3.2. Hybrid core–shell nanoparticles optical simulation based on 10 nm × 41 nm AuNR

In the initial simulations, a hybrid core-shell nanoparticle was modelled, comprising a 10nm × 41nm AuNR core enveloped by $SiO_2@Fe_3O_4$, with 50 nm silicon thickness, and 10 nm Fe_3O_4 thickness. We used Fe_3O_4 thicknesses smaller than 30 nm because they exhibit superparamagnetic; if not, they display ferromagnetic properties [31,32]. This configuration is depicted in Figure 6(a). Observations revealed that the integration of $SiO_2@Fe_3O_4$ shell induces a redshift in λ_{SPR}, from 810 nm to λ_{SPR} = 880 nm. Relative to the solitary AuNR, there is a slight increase in both field enhancement and Q_h, also a slight decrease in the optical cross-sections especially for 50nm SiO_2 thickness but it becomes closer to the AuNR values with increasing SiO_2 thickness and the total volume of hybrid NP. A small distribution of total power dissipation density on the Fe_3O_4 layer can be seen for 50nm SiO_2 thickness.

Subsequent modifications involved escalating the SiO_2 layer's thickness to 60 and 70 nm (Figure 6(b) and 6(c). The analysis reveals that 10 nm increment in SiO_2 thickness results in 10 nm reduction in the redshift of λ_{SPR}. For instant, 60 nm SiO_2 layer exhibits a decrease in λ_{SPR} from 880 nm to 870 nm, and 60 nm SiO_2 layer shows further reduction from 870 nm to 860 nm. Moreover, there is an increase in optical cross-sections for 50nm and 60 nm SiO_2 layers, which approaches the measurements of AuNR. However, the field enhancement and the total power dissipation density decreases with increasing SiO_2 thickness.

Figure 7 presents a comparative analysis of the absorption cross-section and power absorbed across varying SiO_2 thicknesses. It is obvious that the values of absorption cross-section and power absorbed by hybrid nanoparticles with different SiO_2 thicknesses are slightly different.

In the subsequent phase of our research, we augmented the Fe_3O_4 thickness to 15 nm for the hybrid nanoparticle, which previously featured different silicon thicknesses. Figure 8 shows the variations in absorption, scattering, and extinction cross-section associated with the hybrid nanoparticle that incorporates a 15 nm Fe_3O_4 and 50, 60, and 70 nm SiO_2.

The results show that 5 nm increase in Fe_3O_4 thickness (from 10 nm to 15 nm) causes 10 nm redshift in λ_{SPR} (from 880 nm to 890nm) for 50 nm SiO_2 thickness and it remains constant for higher SiO_2 layers. This increase in Fe_3O_4 layer has also slightly reduced the field enhancement and total power dissipation density compared to 10 nm Fe_3O_4 layer. Figure 9(a) and Figure 9(b) specifically showcase the absorption cross-section and power absorbed by hybrid nanoparticle Fe_3O_4 layer of 15 nm and different SiO_2 thicknesses.

Figure 10(a) and Figure 10(b) delineates the σ_{abs} and Q_{abs} for the respective thicknesses. The σ_{abs} of 50 nm $SiO_2@10$ nm Fe_3O_4 hybrid nanoparticle is slightly different from the ones with 50 nm $SiO_2@15$ nm Fe_3O_4 but these two hybrid nanoparticles have a significant difference in Q_{abs}. These values are higher for 50 nm $SiO_2@10$nm Fe_3O_4 than the other one. Also, the absorption cross-section peak for AuNR@50 nm $SiO_2@10$nm Fe_3O_4 occurs at a lower wavelength and closer to λ_{SPR} of AuNR. The same results are valid for 60 and 70 nm SiO_2 layers.
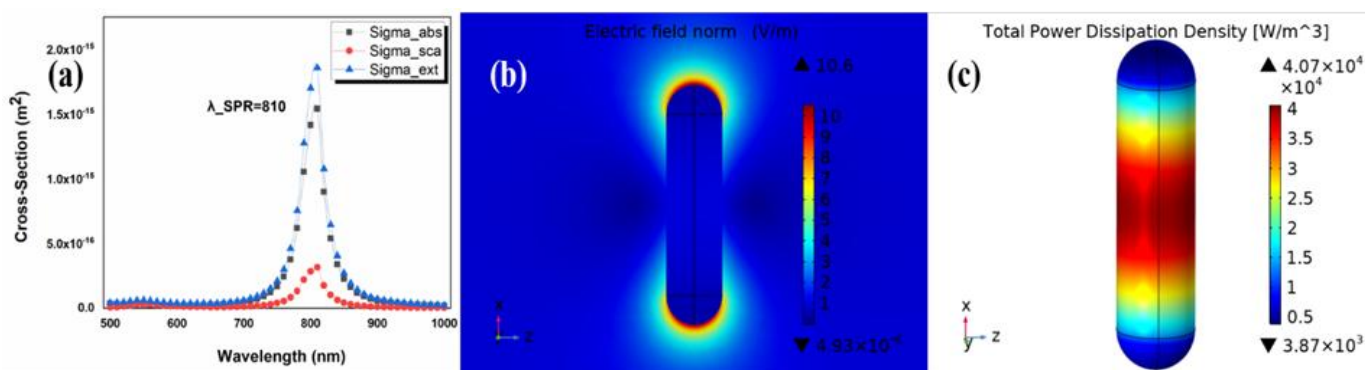
Fig. 5. (a) The optical cross-sections, (b) the volume plot of field enhancement, and (c) the Q_h for 10nm × 41nm AuNR.
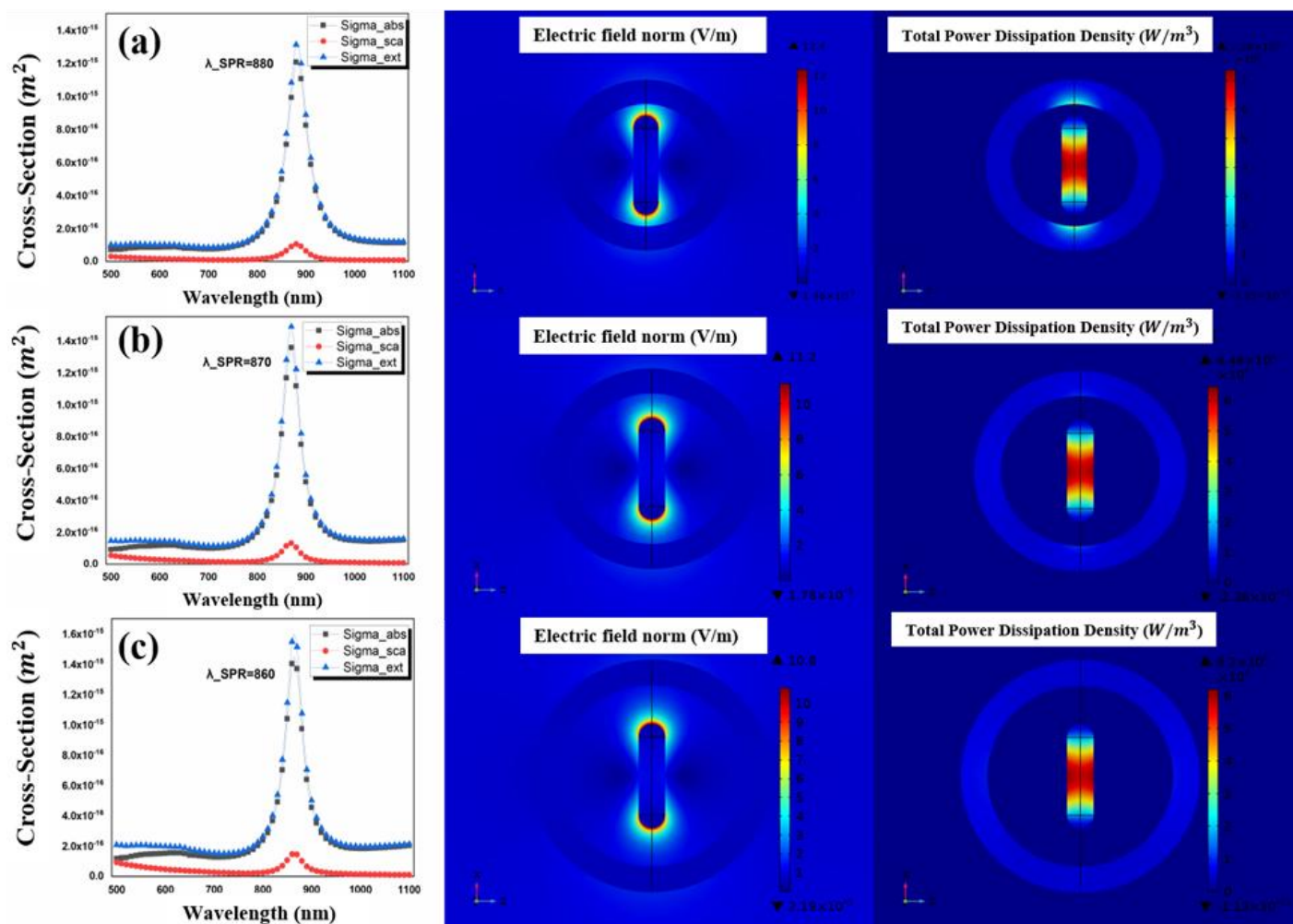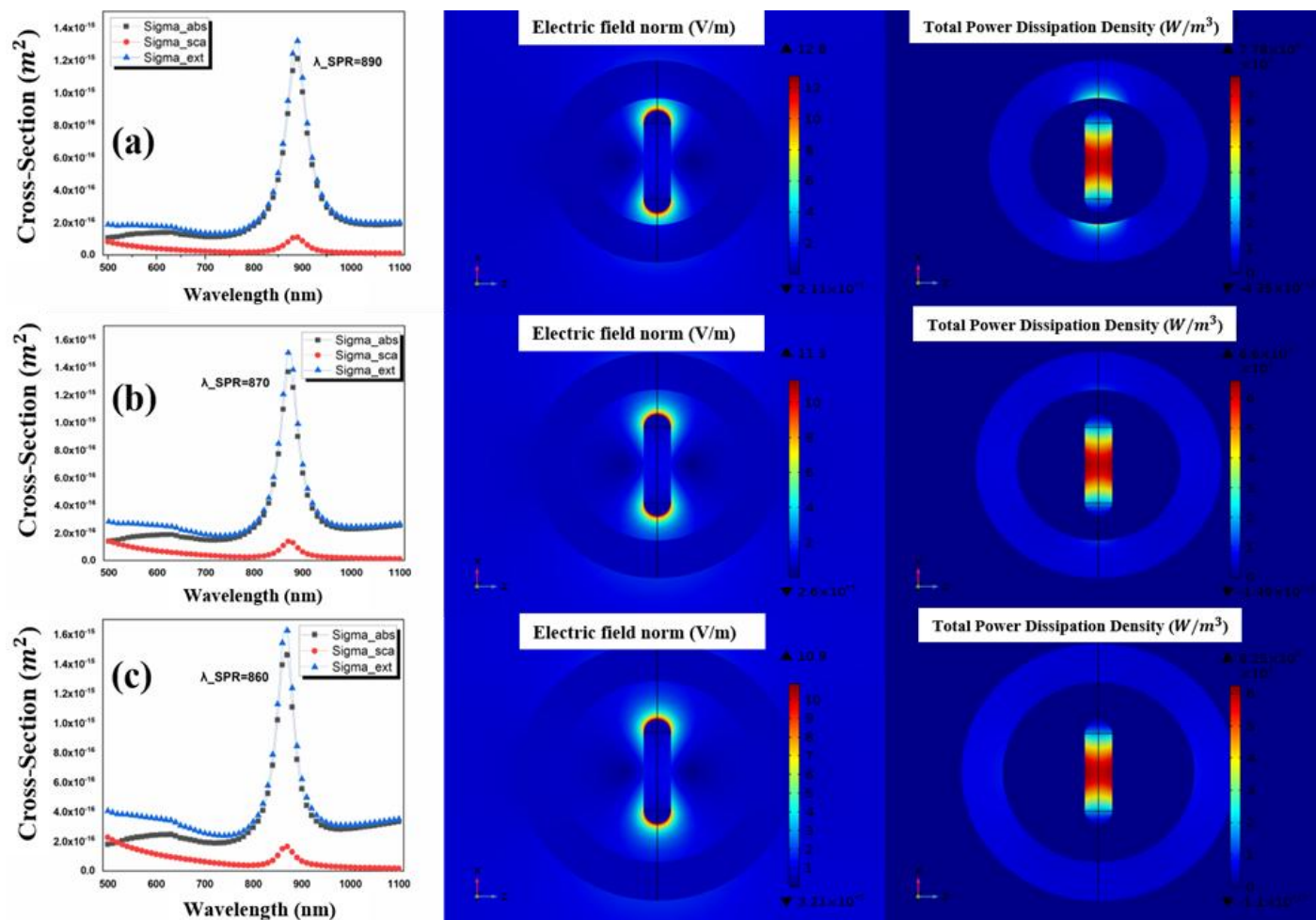
Fig. 6. The optical cross-sections, the field enhancement, and the total power dissipation density of 10nm × 41nm AuNR@SiO$_2$@10 nm Fe$_3$O$_4$ for (a) 50 nm SiO$_2$, (b) 60 nm SiO$_2$, and (c) 70 nm SiO$_2$, respectively.
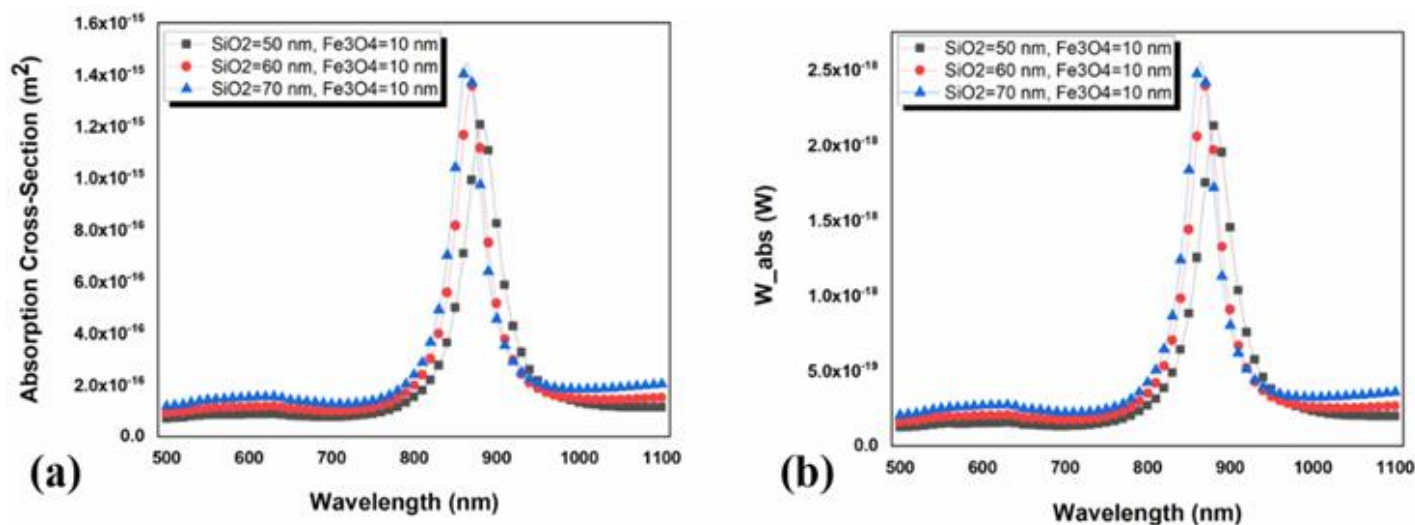
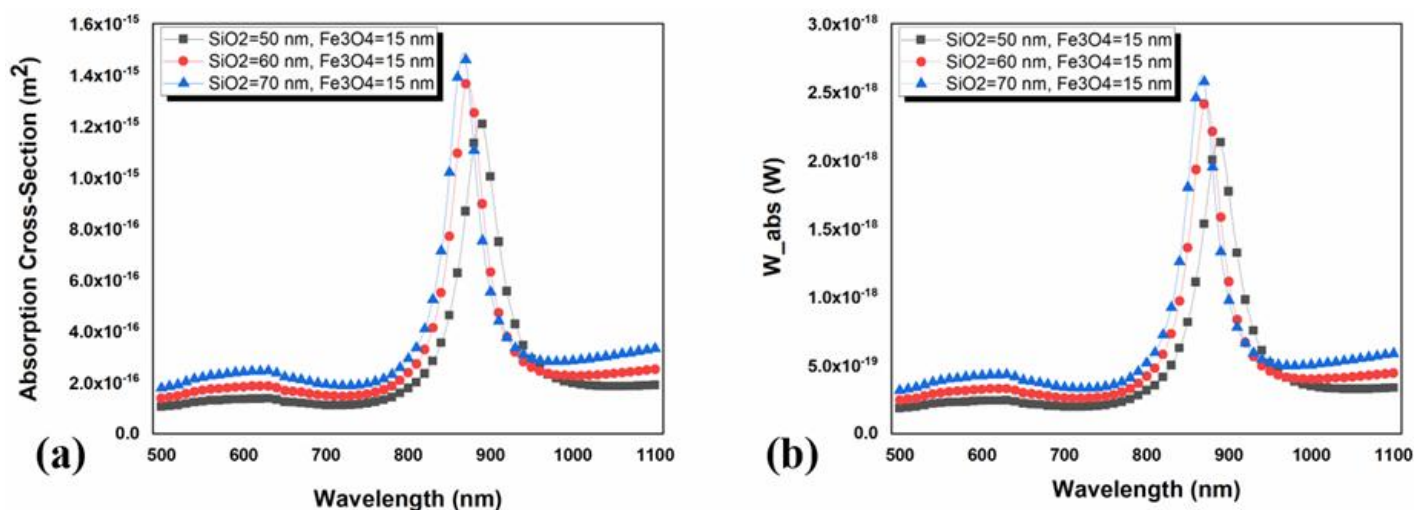**Fig. 7.** The comparison on a) absorption cross-section and b) the power absorbed by Au@ SiO$_2$@ Fe$_3$O$_4$ hybrid core-shell with 10 nm Fe$_3$O$_4$ and different SiO$_2$ thicknesses.

Fig. 8. The optical cross-sections, the field enhancement, and the total power dissipation density of 10nm × 41nm AuNR@SiO$_2$@15 nm Fe$_3$O$_4$ for a) 50 nm SiO$_2$, b) 60 nm SiO2, and c) 70 nm SiO$_2$, respectively.

Fig. 9. The comparison on a) absorption cross-section and b) the power absorbed by Au@SiO$_2$@Fe$_3$O$_4$ hybrid core-shell with 15 nm Fe$_3$O$_4$ and different SiO$_2$ thicknesses.

Since Q$_{abs}$ is an important factor, using as the heat source, we choose the two higher values that belong to 50 nm SiO$_2$@ 10 nm Fe$_3$O$_4$ hybrid nanoparticle and to 60 nm SiO$_2$@ 10 nm Fe$_3$O$_4$ hybrid nanoparticle.

3.3. Hybrid core–shell nanoparticles simulation based on 15nm × 52.5nm AuNR

Subsequent analyses were conducted to ascertain the λ_{SPR}, the absorption, scattering, and extinction cross-sections for the nanoparticle, following the adjustment of the gold nanorod's size to 15 nm × 52.5 nm AuNR. These results are exhibited in Figure 11, which clearly indicates a tripling of all cross-section values in comparison to the 10 nm × 41 nm AuNR. The blueshift of 50 nm from 810 to 760 nm can be seen for this AuNR. This can be a positive point because by applying the $SiO_2@$ Fe_3O_4 shell, the λ_{SPR} is closer to 808 nm compare to the hybrid nanoparticle with 10 nm × 41 nm AuNR. Despite observing a reduction in both field enhancement and Q_h compared to 10 nm × 41 nm AuNR, the enlargement of AuNR core.

3.4. Hybrid core–shell nanoparticles heating

We have shown that 10nm × 41nm AuNR@50nm $SiO_2@$ 10 nm Fe_3O_4, 10nm × 41nm AuNR@60nm $SiO_2@$ 10 nm Fe_3O_4, and 15nm × 52.5nm AuNR@60nm $SiO_2@$10 nm Fe_3O_4 have the highest values among other structures, as the next step we will obtain the temperature change in each particle resulting from the absorbed power under 808 nm laser illumination with an irradiance of 1 mw/μm^2. The Q_{abs} of particles will be serve as the heat source in the Equation 9. The heat map of AuNRs and hybrid core–shell nanoparticles are shown in Figure 15 and Figure 16. As expected, since the 15nm × 52.5nm AuNR absorbed the higher amount of power (Figure 14(b)), it reaches the higher temperature (70.8℃) in comparison to the 10nm × 41nm AuNR (56.4℃).

In Figure 16(a) and Figure 16(b), it can be seen that the incorporation of 50 nm and 60 nm $SiO_2@Fe_3O_4$ shell onto the 10nm×41nm AuNR core result in a decrease of the temperature of the AuNR from 56.4℃ to 41.9℃ while the outer surface of the nanoparticles is around 41.4℃ and 41.3℃, respectively. This reduction is attributed exclusively to the decrease in Q_{abs} for hybrid NP compared to AuNR.
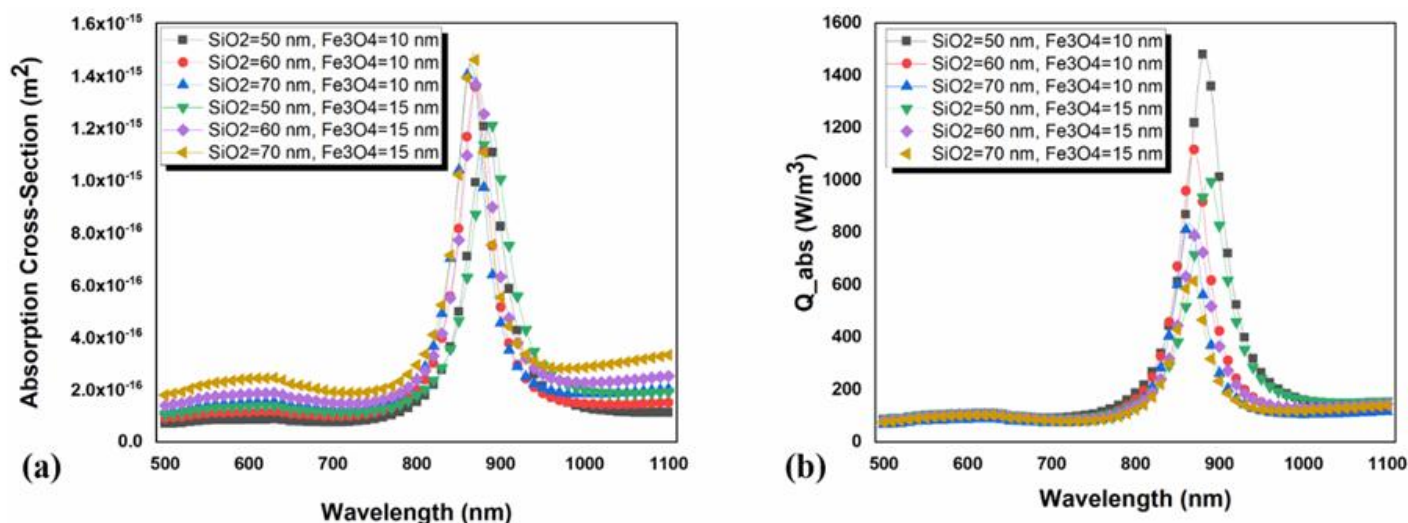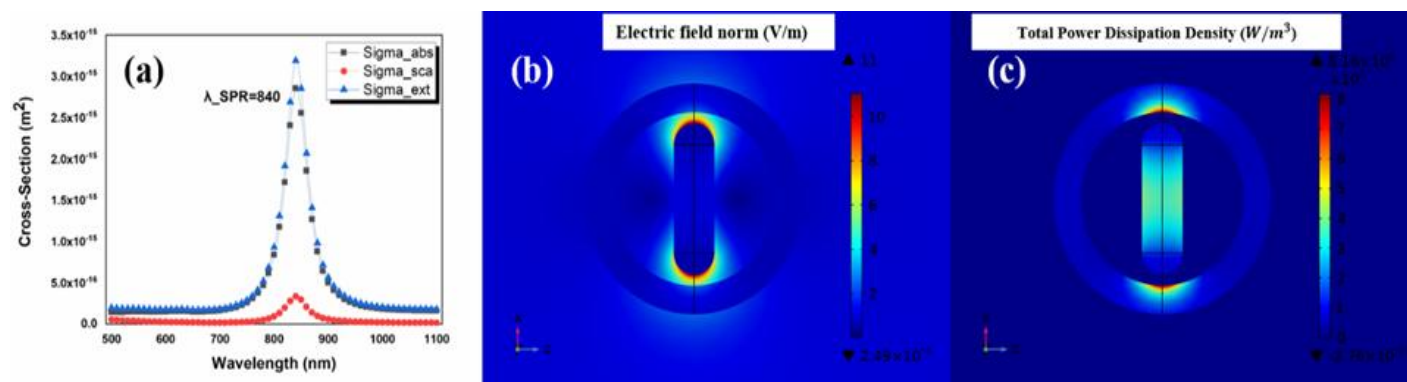

Fig. 10. The comparison on (a) $\sigma_{abs,}$ and (b) Q_{abs} (W_{abs}/V) for Au@SiO_2@Fe_3O_4 hybrid core-shell with 10 nm, and 15 nm Fe_3O_4 and different SiO_2 thicknesses.
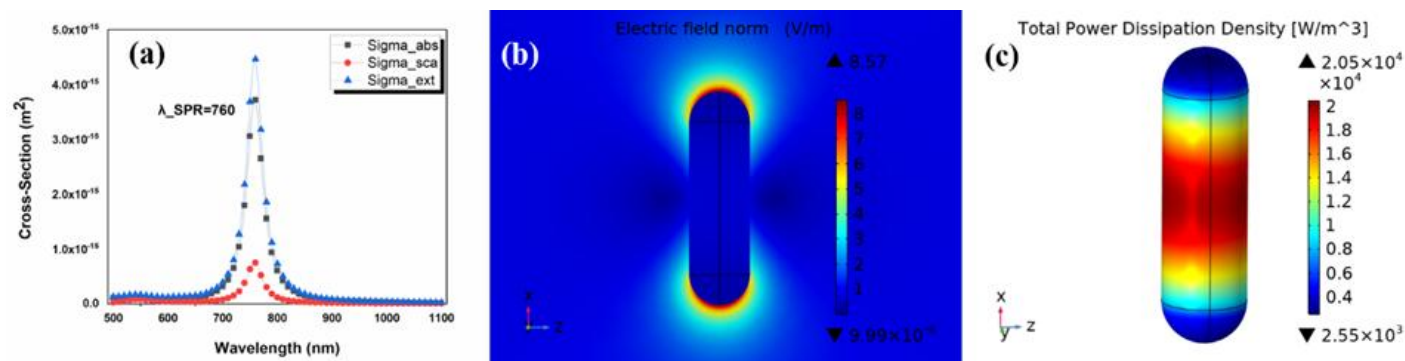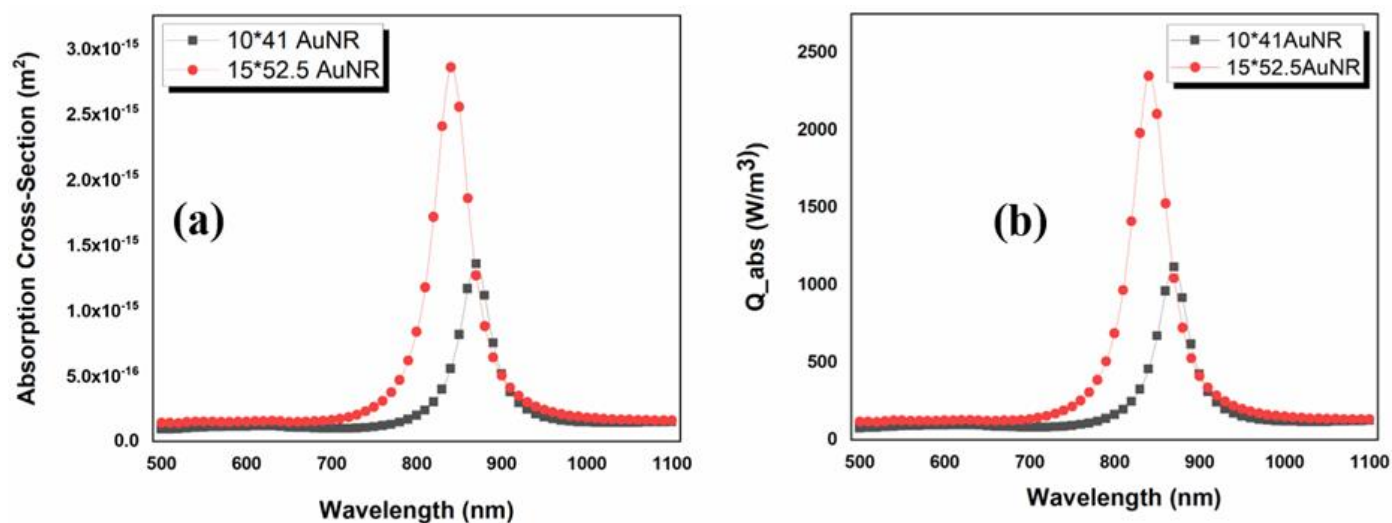

Fig. 11. (a) The optical cross-sections, (b) the volume plot of field enhancement, and (c) the Q_h for 15nm × 52.5 nm AuNR.
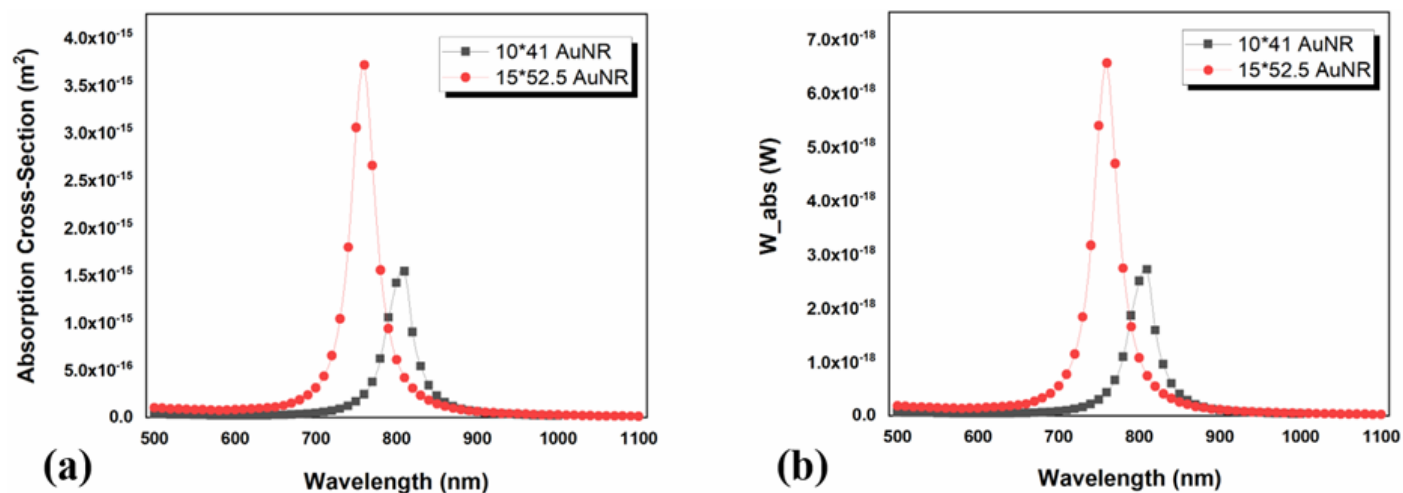
Fig. 12. The comparison of a) the absorption cross-section and b) the power absorbed of 10nm × 41nm AuNR and 15 nm × 52.5 nm AuNR.

Fig. 13. (a) The optical cross-sections, (b) the surface plot of field enhancement, and (c) the Q_h for 15nm × 52.5nm AuNR@60 nm SiO_2@10 nm Fe_3O_4.
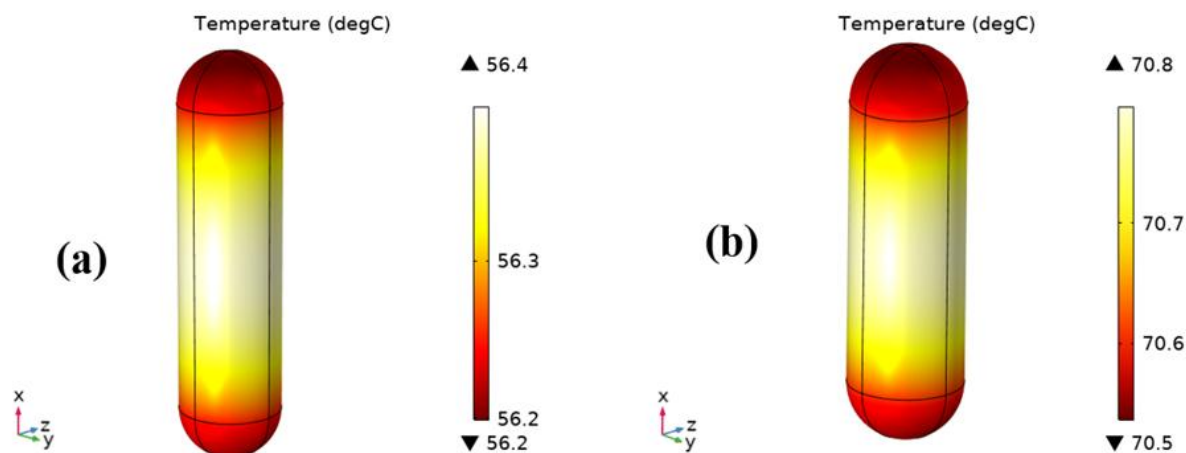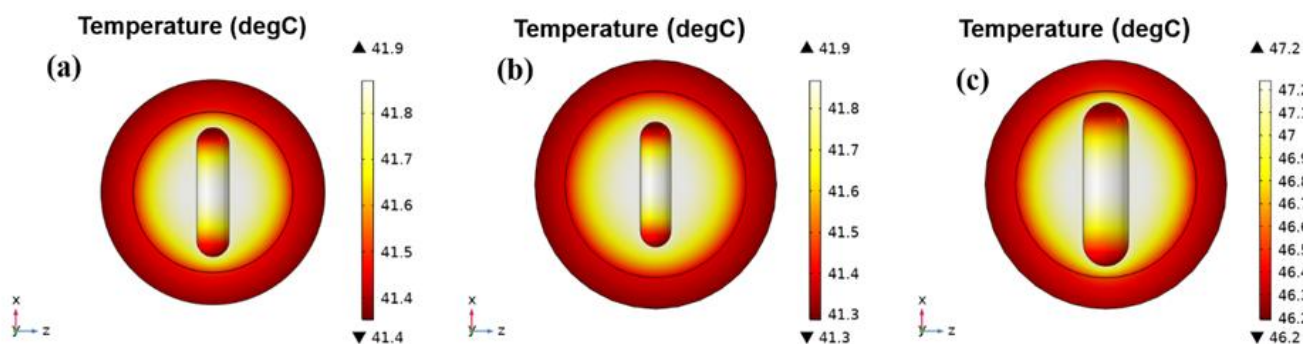

Fig. 14. The comparison of (a) the absorption cross-section, and (b) Q_{abs} for 10 nm × 41 nm AuNR@60 nm SiO_2@10 nm Fe_3O_4 and 15 nm × 52.5 nm AuNR@60nm SiO_2@10 nm Fe_3O_4.

Fig. 15. The steady-state temperature maps of (a) 10nm × 41 nm AuNR, and (b) 15 nm × 52.5 nm AuNR.

Fig. 16. The steady-state temperature maps of (a) 10 nm × 41 nm AuNR@50 nm SiO$_2$@10 nm Fe$_3$O$_4$, (b) 10 nm × 41 nm AuNR@ 60 nm SiO$_2$@10 nm Fe$_3$O$_4$, and (c) 15 nm × 52.5 nm AuNR@60 nm SiO$_2$@10 nm Fe$_3$O$_4$.

Table 2. The absorbed power per unit volume for different AuNRs and hybrid core–shell nanoparticle, and the maximum temperature reached.

Nanoparticle Type	Q_{abs} (W/m^3)	Max. Temperature (℃)
10 × 41 AuNR	5.3E+17	56.4
15 × 52.5 AuNR	4.4E+17	70.8
10 × 41 AuNR@50nm SiO$_2$@10nm Fe$_3$O$_4$	6.7E+15	41.9
10 × 41 AuNR@60nm SiO$_2$@10nm Fe$_3$O$_4$	5.06E+15	41.9
15 × 52.5 AuNR@60nm SiO$_2$@10nm Fe$_3$O$_4$	1.06E+16	47.2

4. CONCLUSION

In conclusion, our comprehensive study delved into the optical cross-sections and thermal generation capabilities of AuNR@SiO$_2$@Fe$_3$O$_4$ hybrid core-shell nanoparticles, focusing on the influence of varying core and shell size. As validation, the initial phase involved the simulation of 10nm × 41nm AuNR with λ$_{SPR}$=808 nm synthesized by Alrahili et al. Furthermore, using this shell on the 15nm × 52.5nm AuNR core leads to a lowered temperature of the AuNR from 70.8℃ to 47.2℃, while the shell itself attains a temperature

of approximately 46.2℃ (refer to Figure 13(c) for observing a distribution of total power dissipation density on the Fe$_3$O$_4$ layer). Consequently, it can be deduced that the second hybrid core–shell nanoparticle with 15nm × 52.5nm AuNR core exhibits enhanced thermal performance in comparison to two other ones and it is the proper candidate for hyperthermia. The Q$_{abs}$ and maximum temperatures reached by 10nm × 41nm AuNR, 15nm × 52 nm AuNR, and hybrid core–shell nanoparticle with different core and shell sizes are reported in Table 2. The λ$_{SPR}$=810 nm simulated by COMSOL Multiphysics demonstrates a close correlation

with the synthesized value. Subsequent simulations utilized this AuNR as a core, encased within $SiO_2@10$ nm Fe_3O_4 shell with 50-60 and 70 nm SiO_2 thickness. The λ_{SPR} measurements revealed a redshift, with a shift of 70 nm for 50 nm SiO_2 thickness, 60 nm for 60 nm SiO2 thickness, and 50 nm for 70 nm SiO_2 thickness. Increased redshift of 80 nm for the 50 nm SiO_2 thickness, while maintaining consistency for the larger shell sizes. The optical properties including absorption cross-section, scattering, and extinction, were recorded between 12E-16 m^2 and 15E-16 m^2 with absorbed power values ranging from 22E-18 ω to 25E-18 ω. The absorbed power per unit volume (Q_{abs}), serving as a heat source, was most pronounced for structures with a 10 nm $SiO_2@Fe_3O_4$ thickness of 60 and 50 nm. The thermal analysis was particularly revealing, with the temperature profiles of the nanoparticles providing critical insights. In an extension of the study, the core size was increased to 15nm × 52.5nm AuNR, with aspect ratio of 3.5, and paired with a 60 nm $SiO_2@$ 10 nm Fe_3O_4 shell. Initial assessments of the optical cross-sections and λ_{SPR} for an uncoated AuNR showed a blueshift from 810 to 760 nm. The absorption cross-section value had an enhancement from 16E-16 m^2 for 10nm × 41nm AuNR to 37E-16 m^2 for 15nm × 52.5nm AuNR. The application of the shell further adjusted the λ_{SPR} from 870 nm to 840 nm, aligning more closely with the target wavelength of 808 nm compared to other structures. The culmination of the research was the thermal profiling of the three selected structures, utilizing the Q_{abs}. Prior to shell application, the 10nm × 41nm AuNR and 15 nm × 52.5 nm AuNR exhibited maximum temperatures of 56.4℃ and 70.8℃, respectively, indicating a superior absorbed power and absorption cross-section for the latter. The incorporation of the 50 nm $SiO_2@10$ nm Fe_3O_4 and 60 nm $SiO_2@10$ nm Fe_3O_4 shells resulted in a temperature reduction on the AuNR to 41.9℃, with the outer surface temperatures registering at 41.4 and 41.3℃, respectively. However, the application of the 60 nm $SiO_2@$ 10 nm Fe_3O_4 shell on the 15nm × 52.5nm AuNR decreased its temperature from 70.8°C to 47.2℃ on the AuNR surface and to 46.2℃ on the outer shell surface. Given that the final temperature of 46.2℃ is within the therapeutic range for hyperthermia, we can deduce that the 15nm ×52.5nm AuNR@60 nm $SiO_2@10$ nm Fe_3O_4 hybrid nanoparticle is a more viable option for hyperthermia applications when compared to the other structures investigated. This conclusion is supported by the enhanced optical properties and the optimal thermal profile achieved by this particular nanoparticle configuration.

DECLARATIONS

Ethical Approval

We affirm that this manuscript is an original work, has not been previously published, and is not currently under consideration for publication in any other journal or conference proceedings. All authors have reviewed and approved the manuscript, and the order of authorship has been mutually agreed upon.

Availability of data and material

All of the data obtained or analyzed during this study is included in the report that was submitted.

Conflicts of Interest

The authors declare that they have no financial or personal interests that could have influenced the research and findings presented in this paper. The authors alone are responsible for the content and writing of this article.

Authors' contributions

All authors contributed equally in the preparation of this manuscript.

REFERENCES

[1] Ijff, M., Crezee, J., Oei, A. L., et al., **2022**. The role of hyperthermia in the treatment of locally advanced cervical cancer: a comprehensive review. *International Journal of Gynecological Cancer*, 32, pp.288-296.

[2] Yi, G., Kim, M. J., Kim, H. I., et al., **2022**. Hyperthermia treatment as a promising anti-cancer strategy: therapeutic targets, perspective mechanisms and synergistic combinations in experimental approaches. *Antioxidants (Basel)*, 11, p.625.

[3] Darvishi, V., Navidbakhsh, M., Amanpour, S., **2022**. Heat and mass transfer in the hyperthermia cancer treatment by magnetic nanoparticles. *Heat and Mass Transfer*, 58, pp.1029-1039.

[4] Báez, D. F., **2023**. Graphene-based nanomaterials for photothermal therapy in cancer treatment. *Pharmaceutics*, 15,p. 2286.

[5] Yue, J., Miao, P., Li, L., et al., **2022**. Injectable carbon dots-based hydrogel for combined photothermal therapy and photodynamic therapy of cancer. *ACS Applied Materials & Interfaces*, 14, pp. 49582-49591. https://doi.org/10.1021/acsami.2c15428.

[6] Ghobadi Alamdari, S., Amini, M., Jalilzadeh, N., et al., **2022**. Recent advances in nanoparticle-based photothermal therapy for breast cancer. *Journal of Controlled Release*, pp.269-303.

[7] Villuendas, H., Vilches, C., Quidant, R., **2022**.

Influence of cell type on the efficacy of plasmonic photothermal therapy. *ACS Nanosci*, 2, pp.494-502.

[8] Gu, W., Hua, Z., Li, Z., et al., **2022**. Palladium cubes with Pt shell deposition for localized surface plasmon resonance enhanced photodynamic and photothermal therapy of hypoxic tumors. *Biomaterials Science*, 1, pp.216-226.

[9] Monk, B. J., Tan, D. S. P., Hernández Chagüi, J. D., et al., **2022**. Proportions and incidence of locally advanced cervical cancer: a global systematic literature review. *International Journal of Gynecological Cancer*, 32, pp.1531-1539.

[10] Hayakawa, Y., Furuya, M., Tahara, H., Kosuge, Y., Kimura, T., Sugawa, K. and Otsuki, J., **2022.** Modulation Technique of Localized Surface Plasmon Resonance of Palladium Nanospheres by Coating with Titanium Dioxide Shell for Application to Photothermal Therapy Agent. *Nanoscale Research Letters*, 17(1), p.60.

[11] Chen, J., Gong, M., Fan, Y., et al., **2022**. Collective plasmon coupling in gold nanoparticle clusters for highly efficient photothermal therapy. *ACS Nano*, 16, pp.910-920.

[12] Dheyab, M. A., Abdul Aziz, A., Moradi Khaniabadi, P., et al., **2023**. Gold nanoparticles-based photothermal therapy for breast cancer. P*hotodiagnosis and Photodynamic Therapy*, 42, p.103312.

[13] Chuang, Y. C., Lee, H. L., Chiou, J. F., et al., **2022**. Recent advances in gold nanomaterials for photothermal therapy. *Journal of Nanotheranostics*, 3, pp.117-131.

[14] Khaksar Jalali, M., Salmani, S., Karimzadeh, L., et al., **2023**. Photothermal treatment of glioblastoma cells based on plasmonic nanoparticles. *Lasers in Medical Science*, 38.

[15] Guo, X., Qi, S., Liu, T., et al., **2022**. Intelligent gold nanoparticles for synergistic tumor treatment via intracellular Ca^{2+} regulation and resulting on-demand photothermal therapy. *Chemical Engineering Journal*, 433, p.133850.

[16] Depciuch, J., Stec, M., Maximienko, A., et al., **2022**. Size-dependent theoretical and experimental photothermal conversion efficiency of spherical gold nanoparticles. *Photodiagnosis and Photodynamic Therapy*, 39, p.102979.

[17] Rahbar Farzam, O., Mehran, N., Bilan, F., et al., **2023**. Nanoparticles for imaging-guided photothermal therapy of colorectal cancer. *Heliyon*, 9, p.e21334.

[18] Wang, H., Wu, Y., Zou, H., et al., **2023**. Photothermal therapy with Ag nanoparticles in mesoporous polydopamine for enhanced antibacterial activity. *ACS Applied Nano Materials*, 6, pp.4834-4843.

[19] Shipunova, V. O., Belova, M. M., Kotelnikova, P. A., et al., **2022**. Photothermal therapy with HER2-targeted silver nanoparticles leading to cancer remission. *Pharmaceutics*, 14, p. 1013.

[20] Marghani, B. H., Fehaid, A., Ateya, A. I., et al., **2022**. Photothermal therapeutic potency of plasmonic silver nanoparticles for apoptosis and anti-angiogenesis in testosterone-induced benign prostate hyperplasia in rats. *Life Sciences*, 291, p.120240.

[21] Niknam, S., Dehdast, S. A., Pourdakan, O., et al., **2022**. Tungsten disulfide nanomaterials (WS₂ NM) application in biosensors and nanomedicine: a review. *Nanomedicine Research Journal*, 7, pp.214-226.

[22] Santhosh, M. V., Geethu, R., Devaky, K. S., **2023**. Solvothermal synthesis of WS₂ rectangular nanoplates and their application in photothermal therapy. *Journal of Materials Science: Materials in Electronics*, 34.

[23] Salimi, M., Shokrgozar, M. A., Delavari, H., et al., **2022**. Photothermal properties of two-dimensional molybdenum disulfide (MoS₂) with nanoflower and nanosheet morphology. *Materials Research Bulletin*, 152, p.111837.

[24] Zhou, Z., Li, X., Hu, T., et al., **2022**. Molybdenum-based nanomaterials for photothermal cancer therapy. *Advanced NanoBiomed Research*, 2, p.2200065.

[25] Tian, Y., Ding, Z., Zheng, X., et al., **2023**. Porphyrin-based porous organic polymer coated ZIF-8 nanoparticles as tumor targeted photosensitizer for combination cancer photodynamic/photothermal therapy. *Microporous and Mesoporous Materials*, 355, p.112562.

[26] Liu, Y., Wang, Z., Gao, Z., et al., **2022**. Porous organic polymer overcomes the post-treatment phototoxicity of photodynamic agents and maintains their antitumor efficiency. *Acta Biomaterialia*, 150, pp.254-264.

[27] Encarnacion, C., Jungwirth, F., Vila Liarte, D., et al., **2023**. Hybrid core–shell nanoparticles for cell-specific magnetic separation and photothermal heating. *Journal of Materials Chemistry B*, 11, pp. TBD.

[28] Abadeer, N., Murphy, C., **2016**. Recent Progress in Cancer Thermal Therapy using Gold Nanoparticles. *The Journal of Physical Chemistry C*, 120, pp.4691-4716.

[29] Sargsian, T. A., Vinnichenko, M. Y., & Hayrapetyan, D. B. **2024**. Modelling the optical properties of gold nanoparticles using COMSOL Multiphysics: Influence of geometry, environment, and temperature. *MatSci Express*, 1(4), 278–290.

[30] Borah, R., Verbruggen, S., **2019**. Coupled Plasmon Modes in 2D Gold Nanoparticle Clusters and Their Effect on Local Temperature Control. *The Journal of Physical Chemistry C*, 123, pp.30594-30603.

[31] Alrahili, M., Peroor, R., Savchok, V., et al., **2020**. Morphology Dependence in Photothermal Heating of Gold Nanomaterials with Near-Infrared Laser. *The Journal of Physical Chemistry C*, 124, pp.4755-4763.

[32] Zargar, F. A., Bhat, H. A., Zargar, M. A., & Malik, S. A. **2024**. Magnetic nanoparticles in cancer thermotherapy: A mathematical approach to optimal treatment design. *MatSci Express*, 1(2), 116–124

[33] Kwizera, E., Chaffin, E., Wang, Y., et al., **2017**. Synthesis and Properties of Magnetic-Optical Core-Shell Nanoparticles. *RSC Advances*, 7, pp.4691-4716.

[34] Bedoya, S. M., Moreau, C., Patel, S., **2019**.

Computational Modeling of Nanoparticle Heating for Treatment Planning of Plasmonic Photothermal Therapy in Pancreatic Cancer. Conference Paper.

[35] Bedoya, S. M., Moqueet, M. A., Lopez, P., et al., **2020**. Multiphysics Modeling of Plasmonic Photothermal Heating Effects in Gold Nanoparticles and Nanoparticle Arrays. *The Journal of Physical Chemistry C*, 124, pp.17172-17182.

[36] Pratap, D., Shah, R. K., Khandekar, S., et al., **2022**. Photothermal Effects in Small Gold Nanorod Aggregates for Therapeutic Application. *Applied Nanoscience*, 12, pp.2045-2058.

[37] Terres-Harro, J. M., Monreal-Trigo, J., Hernández-Montoto, A., et al., **2023**. Finite Element Models of Gold Nanoparticles and Their Suspensions for Photothermal Effect Calculation. *Bioengineering*, 10, p.0232.

[38] Rossi, F., Ratto, F., Pini, R., **2012**. Laser Activated Gold Nanorods for the Photothermal Treatment of Cancer. COMSOL Conference Paper.

[39] Silica: Silicon Dioxide (SiO_2), **2001**. *AZO Materials*.

[40] Horia, H., Easawi, K., Khalil, R., et al., **2020**. Optical and Thermophysical Characterization of Fe_3O_4 Nanoparticles. *IOP Conference Series: Materials Science and Engineering*, 956, p.012016.